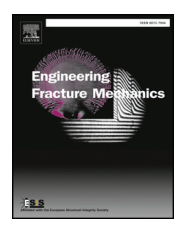
FISEVIER

Contents lists available at ScienceDirect

Engineering Fracture Mechanics

journal homepage: www.elsevier.com/locate/engfracmech



Block cracking in surface coatings of polymeric substrates

Xin He^{a,*}, Ross Larsen^a, Fangliang Chen^b, Huiming Yin^b



- ^a Computational Science Center, National Renewable Energy Laboratory, 15013 Denver W Pkwy, Golden, CO 80401, United States
- ^b Department of Civil Engineering and Engineering Mechanics, Columbia University, 610 Seeley W. Mudd 500 West 120th Street, New York, NY 10027, United States

ARTICLE INFO

Keywords:
Coating/substrate system
Stress analysis
Energy release rate
Cracking
Cohesive zone model

ABSTRACT

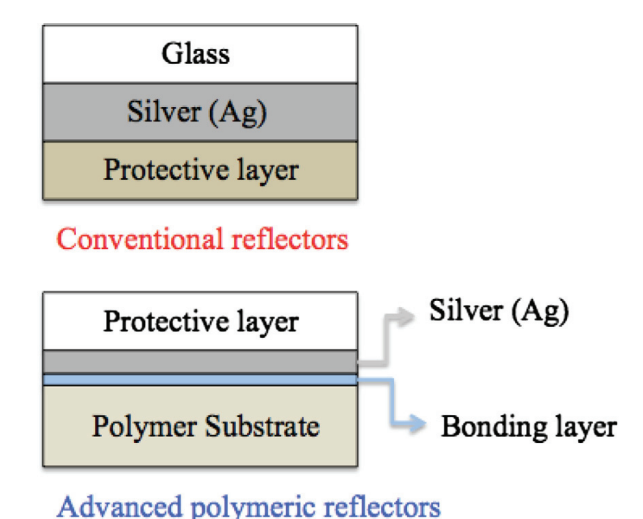
Block cracking is commonly observed in form of a series of interconnected cracks that divide the surface of multilayered materials into approximately rectangular or square pieces. A three-dimensional (3D) elastic fracture model is developed to study the block cracking in thin film/substrate structures which consist of a thin protective metal oxide coating fully bonded to a polymer substrate. Under a temperature change, fracture occurs in the coating due to the thermal stress caused by the material mismatch. Using the plane assumption and non-shearing assumptions, the displacement and stress fields in this substrate-coating system under thermal loading are explicitly solved and verified with the finite element (FE) simulation results. Therefore, the energy release rate (ERR) can be calculated from the work done by the stress on the crack opening before crack and has been used to study the fracture initiation, infilling and saturation. Additionally, the theoretical fracture analysis results are verified by FE simulation using the cohesive zone model (CZM) and experimental data from literature. The results show that the fracture model presented in this study is able to capture the displacement and stress distributions in the thin hard oxide film fully bonded to a polymer substrate accurately and predicts the fracture initiation, infilling and saturation successfully.

1. Introduction

Due to its advanced mechanical and thermal properties, metal oxide thin film coating of soft structures has been widely used to improve the mechanical and thermal properties of metallic or polymeric materials [1–4]. Such structures are of interest because a light and flexible substrate allows for applications across a variety of form factors and can be more cost effective than with rigid substrates [5–8]. An interesting application for metal oxide coatings on a compliant (polymer) substrate is in protective coatings for silver-coated polymer film reflectors, which have found application in parabolic trough reflectors for concentrating solar power [6,9–11] and in other applications for which a flexible reflector is desirable [12]. In these reflectors, multiple oxide layers may be used both to impart abrasion resistance [6,9,11] or to improve the reflectance through thin-film interference [10]. A schematic example of the construction of such a reflector as a coating/substrate system manufactured by depositing thin metal oxide and metal films on the polymer substrates is shown in Fig. 1. Compared with traditional mirror designs which utilize silver painted on the back of glass, this advanced front surface design attains higher reflectance and lower cost for both manufacture and installation [13]. However, under temperature changes, the brittle metal oxide coating layer on the polymer substrate may suffer premature failure, as shown in Fig. 2 because of cracking due to the significant mismatch in the thermal expansion coefficients of the materials in the stack. As a result, the cracking in the surface layer will cause the loss of its protectiveness and the reduction of its reflectance efficiency.

E-mail address: Xin.He@nrel.gov (X. He).

^{*} Corresponding author.



1

Fig. 1. Schematic silvered polymer reflector designs, after [6,9,13].

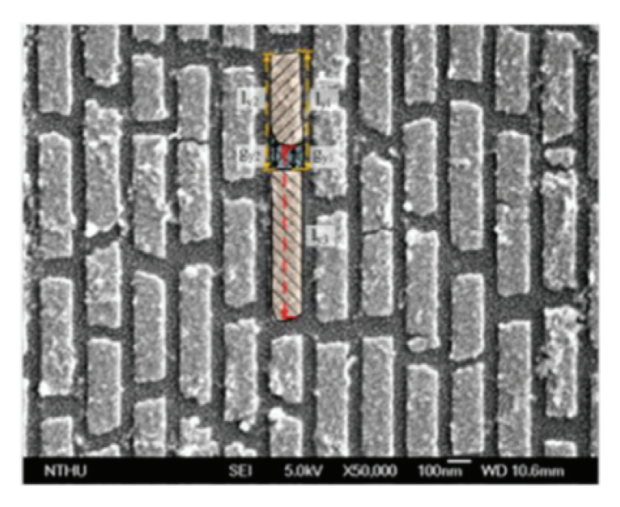


Fig. 2. Nano Metal Crack Initiation on Polymer [14].

Therefore, it is essential to understand the fracture mechanism in this advanced polymeric solar reflector.

Typically, the cracking behaviors of a coating are commonly studied by applying uniaxial tension and bending, owing to their relatively simple testing configurations and well-controlled crack patterns [15-19]. Under tensile loading, opening-mode fractures (OMFs) perpendicular to the applied loading would initiate in the coating [20,21]. In 1992, Nakamura and Kamath [22] presented the results of a three dimensional (3D) finite element (FE) analysis of the mechanics of crack growth and de-cohesion in a highly compliant thin film bonded to a rigid substrate. The computational analysis showed that, in the absence of de-cohesion, the stress intensity factor along the leading edge of the crack reaches a steady state value when the crack length is about twice the film thickness. In addition, the computed results confirmed the existence of high interface stress that may cause de-cohesion. Even though the cracking process itself is 3D, the elastic fields of a steady-state channeling crack in the thin film due to an OMF have been often solved by a two-dimensional (2D) plane strain analysis [20]. Initially, studies of the coating cracking behaviors have focused on the local elastic solution in the neighborhood of the singular point that exists at the crack tip, which is located at the interface between the fractured and intact layers [23–27,15,28–30,17,31]. Although the local solutions are useful in the study of fracture propagation, they cannot be directly used to predict fracture initiation, fracture spacing, or to study the interaction between fractures [32]. According to the studies of Bai and his coworkers [33-35], an overall elastic field in the thin film that is based on the complete set of governing equations for the elastic boundary value problems should be used to completely understand fracture spacing. Later on, Yin and his coworkers proposed a plane strain elastic model [36,37,32,38], where the closed-form elastic solutions in the coating/ substrate structure were obtained and used to interpret fracture initiation, infilling, and saturation caused by tension in the layered materials successfully.

Instead of uniaxial loading, one can consider the case of thermal loading applied to the coating/substrate structures. Here interconnected cracks along both longitudinal and transversal direction would form in the brittle coating driven by the residual stress caused by temperature change dividing the structural component into approximately rectangular pieces. In this case, the 2D plain strain or stress assumptions would not be applicable, therefore, a full 3D analysis is essential. Based on the literature, most studies on

residual stress and 3D fracture analysis of coating/substrate structures under thermal loading are limited experimental measurements [39–42,14], while very seldom theoretical models can be found [43,44,28,45–47]. The details about existing testing methods and theoretical models are summarized as follows.

In order to study the fracture behavior of the coating under thermal loading, the residual stress, which acts as driving force, needs to be measured or analyzed. The most commonly used approach to measure the residual stress in coating is based on the curvature of the elastically deformed coated substrate. When the thickness of the film is small compared to that of the substrate, the following formula proposed by Stoney [39] can be used to predict the residual stress in coating:

$$\sigma_{\chi\chi}^f \approx -E_s \frac{h_s^2}{6h_f R} \tag{1}$$

where E_s is the Young's modulus of substrate, R is the radius of curvature, h_s is the thickness of substrate while h_f is the thickness of coating. The index xx denotes the stress component in direction of the length side of the beam. It was argued by Berry [40] that such a substrate rather curls into an approximately cylindrical shape instead of bowl or cap-like deformation. In this case, the plate modulus should be used to replace E_s . Later, Ohring [41] found that when measuring thin films deposited on plate-like substrate, the corresponding biaxial deformation has to be taken into account by using the biaxial modulus. In 2006, Schwarzer [42] examined different forms of Stoney's equation by applying a correct 3D FE model and found the biaxial modulus would yield an accurate result while the plate modulus would deliver a bigger stress by 20–30 percent.

In 1995, Evans and Hutchinson [43] presented several models for mechanisms which give rise to tensile stresses in thin film deposition, and gave the expression of residual stress in thin film which is attached to a infinite substrate. Later, Hutchinson [44] proposed a form for residual stress in thin coating for the case where the substrate can expand or shrink freely based on the assumption that the substrate is effectively uninfluenced by the film and the substrate imposes its in-plane strains on the film, which means the shear strain in the film is equal to that in substrate at the area away from the edge. This model can be used to predict the stress in the center area, however, more accurate displacement and stress distributions at the edge are required for cracking analysis. In 2003, Hsueh and Yanaka [28] derived a closed-form analytical solution to predict the stress distribution in a film segment when the film/substrate system was subjected to both residual stresses and tensile loading. In this model, the effects of external loading was incorporated into the shear lag model. Based on the solved stress and displacement, the cracking in coating was predicted by adopting both strength and energy threshold criteria for cracking onset. However, this model only considered the stress along the same direction as external loading while other stresses are ignored. Following the developed theoretical solutions in [28], another study was done by Hsueh and Wereszcazk [48] to calculate the residual stress in the coating based on the multiple coating crack spacing. Based on the force and moment balances, another analytical model was proposed by Zhang et al. [45] to predict the thermal residual stress in multi-layered coating systems. In this model, the total strains of the coating layer and the substrate were decomposed into an in-plane strain and a bending strain, following this a closed-form solution of thermal stresses was obtained, which posses the merit of independence of the number of coating layers. In 2011, Ahmed et al. [46] used the Micro-Raman spectroscopy to access the residual stress in a diamond coating as a function of the strain applied to the ductile substrate. In order to verify the experimental results, a new shear lag model was developed by considering the effect of the substrate plasticity based on Hsueh and Yanaka's work [28]. Recently, Roy and Ghosh [47] proposed another model to predict the residual stress in the free expanded Galvannealed coating/ substrate structure based on the method of superposition. The normal stress in both coating and substrate were obtained. The results showed that the initial thermal residual stress generated in coating is independent of the coating thickness but depends on the temperature difference, inherent mechanical properties of the coating, and thermal properties of the coating and the substrate. Based on the residual stress, the fracture ERRs in the coating along both longitudinal and transversal directions were obtained and used to predict the crack spacing. The experimental verification showed that the predicted crack spacings were quite different from the observed results and the proposed model underestimated the crack spacing. The draw back of this proposed model is that the solved normal strains in coating are constant, which depend on the material properties only. Therefore, it can not capture the strain and stress spacial distribution accurately.

In order to study the residual stress and fracture behavior of the multilayered advanced polymeric reflectors more accurately than with previously applied methods [28,45–47], a 3D elastic fracture model is proposed based on the work done by Yin and his coworkers [38]. As an initial study, we consider a two-layer structure with a metal oxide protective coating and a polymer substrate as the silver and bonding layers are much thinner. Specifically, we limit the problem to be solving the elastic field and analyzing the fracture behavior of the titanium oxide coating with thickness h_f , Young's modulus E^f , Poisson's ratio v^f , and thermal expansion coefficient α_f fully bonded to a polyethylene terephthalate (PET) substrate with thickness h_s , Young's modulus E^s , Poisson's ratio v^s , and thermal expansion coefficient α_s under a temperature change of ΔT . The boundary conditions are set as follows: the displacement along the thickness direction at the bottom of the substrate is fixed while it's free to expand along the length and width direction. Once the temperature change reaches the critical value, OMFs would initiate in the coating layer and propagate toward the interface between the coating layer and the substrate. To simplify things, the length and width of the model are set to be coincident and equal to 2λ as the coating would be cracked into square pieces eventually if the temperature change is high enough. Considering a section between two adjacent OMFs, a simplified model is built and shown in Fig. 3.

The remainder of this paper is organized as follows: Section 2 will develop the general formulation and provide explicit solution of the 3D elastic field in the coating/substrate system. Section 3 will then verify the elastic field predicted by the theoretical model given in Section 2 through comparison to a FE analysis. The fracture analysis based on the obtained elastic field will be presented in Section 4 while the verification of fracture analysis using FE simulation results and experimental data from literature will be provided in

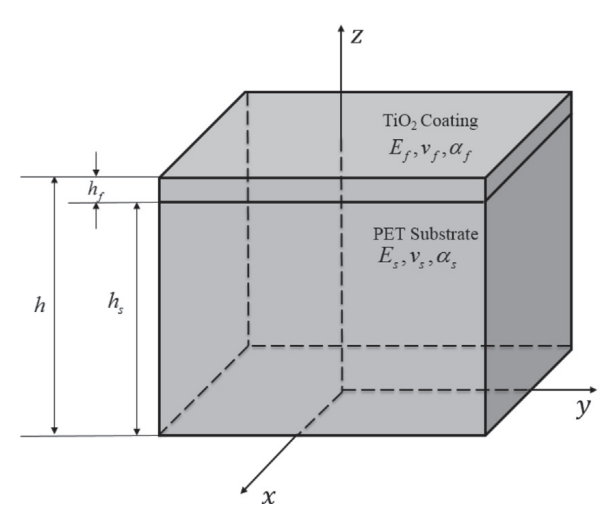


Fig. 3. Schematic illustration of the simplified structures.

Section 5. Finally, some concluding remarks will be given in Section 6.

2. Formulation for 3D elastic field analysis

Assume the displacement is u_x along x-direction, u_y along y-direction, and u_z along z-direction. For the elastic coating and substrate structure, using the small displacement assumption, the stress under a temperature change of ΔT can be written as follows:

$$\sigma_{xx}^{i} = \frac{E^{i}}{(1 + \nu^{i})(1 - 2\nu^{i})} \left[(1 - \nu^{i})u_{x,x}^{i} + \nu^{i}u_{y,y}^{i} + \nu^{i}u_{z,z}^{i} \right] - \frac{\Delta T\alpha_{i}E^{i}}{1 - 2\nu^{i}}$$
(2)

$$\sigma_{yy}^{i} = \frac{E^{i}}{(1+\nu^{i})(1-2\nu^{i})} [(1-\nu^{i})u_{y,y}^{i} + \nu^{i}u_{x,x}^{i} + \nu^{i}u_{z,z}^{i}] - \frac{\Delta T\alpha_{i}E^{i}}{1-2\nu^{i}}$$
(3)

$$\sigma_{zz}^{i} = \frac{E^{i}}{(1+\nu^{i})(1-2\nu^{i})} \left[(1-\nu^{i})u_{z,z}^{i} + \nu^{i}u_{x,x}^{i} + \nu^{i}u_{y,y}^{i} \right] - \frac{\Delta T\alpha_{i}E^{i}}{1-2\nu^{i}}$$

$$\tag{4}$$

$$\tau_{xy}^{i} = \frac{E^{i}(u_{x,y}^{i} + u_{y,x}^{i})}{2(1 + \nu^{i})}$$
(5)

$$\tau_{xz}^{i} = \frac{E^{i}(u_{x,z}^{i} + u_{z,x}^{i})}{2(1 + \nu^{i})}$$
(6)

$$\tau_{yz}^{i} = \frac{E^{i}(u_{y,z}^{i} + u_{z,y}^{i})}{2(1 + \nu^{i})} \tag{7}$$

where the subscript and superscript i = (f, s) denote the coating (f) and substrate (s) layers, respectively. The equilibrium equations expressed in displacement read,

$$\frac{2(1-\nu^{i})}{1-2\nu^{i}}u_{x,xx}^{i}+u_{x,yy}^{i}+u_{x,zz}^{i}+\frac{1}{1-2\nu^{i}}(u_{y,xy}^{i}+u_{z,xz}^{i})=0$$
(8)

$$\frac{2(1-\nu^i)}{1-2\nu^i}u^i_{y,yy} + u^i_{y,xx} + u^i_{y,zz} + \frac{1}{1-2\nu^i}(u^i_{x,xy} + u^i_{z,yz}) = 0$$
(9)

$$\frac{2(1-\nu^i)}{1-2\nu^i}u^i_{z,zz} + u^i_{z,yy} + u^i_{z,xx} + \frac{1}{1-2\nu^i}(u^i_{x,xz} + u^i_{y,yz}) = 0$$
(10)

By following the same principle as in the 2D problem [38,20,21], we assume that the top surface of the coating will stay flat after deformation (plane assumption) and that all lines which were parallel to y-axis or x-axis before deformation will stay parallel to the corresponding axis after deformation. More specifically, the top surface of the structure will remain square after deformation (non-shearing assumption). Mathematically, these assumptions can be expressed as

$$u_{z,x}^i = u_{z,y}^i = 0 (11)$$

and

$$u_{x,y}^i = u_{y,x}^i = 0 (12)$$

Substituting Eqs. (11) and (12) into Eqs. (8)-(10), the equilibrium equations simplify to,

$$\frac{2(1-\nu^i)}{1-2\nu^i}u^i_{x,xx} + u^i_{x,zz} = 0 \tag{13}$$

$$\frac{2(1-\nu^i)}{1-2\nu^i}u^i_{y,yy} + u^i_{y,zz} = 0 \tag{14}$$

$$\frac{2(1-\nu^i)}{1-2\nu^i}u^i_{z,zz} + \frac{1}{1-2\nu^i}(u^i_{x,xz} + u^i_{y,yz}) = 0.$$
(15)

2.1. General solution of the displacement in x-direction

2.1.1. Displacement in the coating (u_x^f)

Eq. (13) is a decoupled partial differential equation of u_x . By applying the method of separation of variables, the general solution of u_x in the coating can be written as,

$$u_{r}^{f} = f(x)g(z) + \varepsilon_{u}x \tag{16}$$

where f(x) is a function of x while g(z) is a function of z, ε_u is used to account for the uniform strain, and the superscript f stands for coating or thin film.

Substituting Eq. (16) into Eq. (13) produces:

$$\frac{2(1-\nu^f)}{1-2\nu^f}\frac{f''}{f} + \frac{g''}{g} = 0\tag{17}$$

Both f and f'' are functions of x and g and g'' are functions of z, so the two terms in Eq. (17) can be linked by an independent constant C^2 .

$$\frac{f''}{f} = -\frac{1 - 2\nu^f}{2(1 - \nu^f)} \frac{g''}{g} = C^2 \tag{18}$$

From Eq. (18), the general solution of u_x^f can be obtained as

$$u_x^f = [a_1 \sinh(Cx) + a_2 \cosh(Cx)][a_3 \sin(\xi_f Cz) + a_4 \cos(\xi_f Cz)] + \varepsilon_u x$$

$$\tag{19}$$

where

$$\xi_f = \sqrt{\frac{2(1 - \nu^f)}{1 - 2\nu^f}} \tag{20}$$

and $a_i(i = 1, 2, 3, 4)$ are constants to be determined.

The symmetry of u_x^f at x = 0 implies

$$u_x^f(x=0) = 0$$
 (21)

and the free shearing boundary condition at the top surface, $\tau_{xz}^f(z=h)=0$ yields

$$u_{x,z}^f(z=h)=0 (22)$$

in which the assumption Eq. (11) has been used.

Applying Eqs. (21) and (22) to Eq. (19) gives

$$a_2 = 0$$
 (23)

$$a_3\cos(\xi_f Ch) = a_4\sin(\xi_f Ch) \tag{24}$$

So the displacement along x-direction in coating is reduced to

$$u_x^f = Asinh(Cx)cos(\xi_f Ch - \xi_f Cz) + \varepsilon_u x$$
(25)

where A, C and ε_u are unknowns to be determined using the boundary conditions.

2.1.2. Displacement in the substrate (u_r^s)

By repeating the same derivation as in Section 2.1.1, the general solution of displacement along x-direction in the substrate, u_x^s , can be written as

$$u_x^s = [b_1 \sinh(Cx) + b_2 \cosh(Cx)][b_3 \sin(\xi_s Cz) + b_4 \cos(\xi_s Cz)] + \varepsilon_u x$$
(26)

where:

$$\xi_s = \sqrt{\frac{2(1 - \nu^s)}{1 - 2\nu^s}} \tag{27}$$

and $b_i(i = 1, 2, 3, 4)$ are constants to be determined.

Similarly, by applying the plane assumption (Eq. (12)), the free shearing stress boundary condition at the bottom, $\tau_{xz}^s(z=0)=0$, can be simplified as

$$u_{x,z}^{s}(z=0) = 0 (28)$$

and the symmetry of u_x^s at x = 0 is

$$u_s^s(x=0) = 0$$
 (29)

Combining Eqs. (28), and (26), the constants b_2 and b_3 reduce to

$$b_2 = 0$$
 (30)

$$b_3 = 0$$
 (31)

so that the general solution of u_x^s becomes

$$u_x^s = Bsinh(Cx)cos(\xi_sCz) + \varepsilon_u x$$
 (32)

Again, B, C and ε_u are unknowns to be determined using the boundary conditions.

2.2. General Solution of Displacement in y-direction

For this special case where the length and width of the structure are the same, the displacement in y-direction can be obtained in the same fashion. Therefore, by replacing x with y and y with x in u_x^f and u_x^s , the displacement along y-direction in the coating and substrate can be obtained:

$$u_y^f = Asinh(Cy)cos(\xi_f Ch - \xi_f Cz) + \varepsilon_u y$$
(33)

$$u_{v}^{s} = Bsinh(Cy)cos(\xi_{s}Cz) + \varepsilon_{u}y$$
 (34)

Notice that here the block cracking exhibits a square pattern, so Eqs. (33) and (34) share the same form as Eqs. (25) and (32), respectively.

2.3. General solution of displacement in z-direction

Once u_x and u_y in both coating and substrate are obtained, the general solution of u_z can be solved based on the equilibrium equation in z-direction,

$$u_{z,zz}^{i} = -\frac{1}{2 - 2\nu^{i}} (u_{x,xz}^{i} + u_{y,yz}^{i})$$
(35)

2.3.1. Displacement in the coating (u_z^f)

Integrating the equilibrium equation along *z*-direction in coating twice, the general solution of displacement along *z*-direction in the coating can be obtained as,

$$u_z^f = -\frac{1}{2 - 2\nu^f} \int_z u_{x,x}^f + u_{y,y}^f dz + f_1(x, y)z + g_1(x, y)$$
(36)

where $f_1(x, y)$ and $g_1(x, y)$ are functions of x and y. Substituting Eq. (25) and (33) into Eq. (36) yields,

$$u_{z}^{f} = \frac{A}{(2 - 2\nu^{f})\xi_{f}} sin(\xi_{f}Ch - \xi_{f}Cz)[cosh(Cx) + cosh(Cy)] - \frac{\varepsilon_{u}z}{1 - \nu^{f}} + f_{1}(x, y)z + g_{1}(x, y) = 0$$
(37)

The free normal stress boundary condition at the top surface of coating is

$$\sigma_{zz}^f(z=h)=0\tag{38}$$

Combining Eqs. (4), (25), (33), (37), and (38), $f_1(x, y)$ can be determined as

$$f_1(x, y) = \frac{1 - 2v^f}{2 - 2v^f} [ACcosh(Cx) + ACcosh(Cy) + 2\varepsilon_u] + \frac{1 + v^f}{1 - v^f} \alpha_f \Delta T.$$
(39)

2.3.2. Displacement in the substrate (u_x^s)

Similarly to Section 2.3.1, the displacement along z-direction in substrate can be written as,

$$u_z^s = -\frac{B}{(2 - 2\nu^s)\xi_s} \sin(\xi_s Cz) [\cosh(Cx) + \cosh(Cy)] - \frac{\varepsilon_u z}{1 - \nu^s} + f_2(x, y)z + g_2(x, y) = 0$$
(40)

where $f_2(x, y)$ and $g_2(x, y)$ are functions of x and y.

Applying the fixed bottom boundary condition,

$$u_z^s(z=0) = 0 (41)$$

 $g_2(x, y)$ can be determined,

$$g_2(x,y) = 0 (42)$$

Next by considering the continuity of u_z and σ_{zz} at the interface,

$$u_{z}^{f}(z=h_{s})=u_{z}^{s}(z=h_{s}),$$
 (43)

and

$$\sigma_z^f(z=h_s) = \sigma_{zz}^s(z=h_s) \tag{44}$$

the unknown functions $g_1(x, y)$ and $f_2(x, y)$ are found to be,

$$f_{2}(x, y) = \frac{E^{f}(1 + v^{s})(1 - 2v^{s})}{E^{s}(1 + v^{f})(2 - 2v^{s})} AC \left[1 - \cos(\xi_{f}Ch_{f})\right] \left[\cosh(Cx) + \cosh(Cy)\right] + \frac{1 + v^{s}}{1 - v^{s}} \alpha_{s} \Delta T + \frac{1 - 2v^{s}}{1 - v^{s}} \varepsilon_{u} + \frac{BC(1 - 2v^{s})}{2(1 - v^{s})} \cos(\xi_{s}Ch_{s}) \left[\cosh(Cx) + \cosh(Cy)\right]$$

$$(45)$$

and

$$g_{1}(x, y) = -\frac{\cosh(Cx) + \cosh(Cy)}{2} \left[\frac{A\sin(\xi_{f}Ch_{f})}{\xi_{f}(1 - \nu^{f})} + \frac{1 - 2\nu^{f}}{1 - \nu^{f}} ACh_{s} + \frac{B\sin(\xi_{s}Ch_{s})}{(1 - \nu^{s})\xi_{s}} \right]$$

$$-\frac{1 + \nu^{f}}{1 - \nu^{f}} \alpha_{f} \Delta Th_{s} - \frac{\varepsilon_{u}h_{s}}{1 - \nu^{s}} + \frac{2\nu^{f}\varepsilon_{u}h_{s}}{1 - \nu^{f}} + f_{2}(x, y)h_{s}$$

$$(46)$$

2.4. Explicit displacement field

The general solutions for u_x , u_y , and u_z have been obtained for both coating and substrate. However, there are still four unknowns (A, B, C, and ε_u) that need to be determined. In the following section, we apply the continuity and boundary conditions to solve for all the unknowns.

2.4.1. Continuity at the Interface

The continuity of displacement u_x and u_y at the interface, $u_x^f(z=h_s)=u_x^s(z=h_s)$ and $u_y^f(z=h_s)=u_y^f(z=h_s)$, yields,

$$A\cos(\xi_f Ch_f) = B\cos(\xi_s Ch_s) \tag{47}$$

and the continuity of shearing stress at the interface, $\tau_{xz}^f(z=h_s)=\tau_{xz}^s(z=h_s)$ and $\tau_{yz}^f(z=h_s)=\tau_{yz}^s(z=h_s)$, yields

$$\frac{AE^f \xi_f}{1 + v^f} \sin(\xi_f Ch_f) = -\frac{BE^s \xi_s}{1 + v^s} \sin(\xi_s Ch_s) \tag{48}$$

By combining Eqs. (47) and (48), we find a function of only the single unknown, C,

$$\frac{E^{f}\xi_{f}(1+v_{s})}{E^{s}\xi_{s}(1+v_{f})}\sin(\xi_{f}Ch_{f})\cos(\xi_{s}Ch_{s}) + \sin(\xi_{s}Ch_{s})\cos(\xi_{f}Ch_{f}) = 0.$$
(49)

By solving this nonlinear equation numerically, the unknown *C* which is a function of material properties and thickness but independent of crack spacing can be determined.

According to [38], many solutions exist for constant C because of the periodicity of the sin() and cos() functions, which suggests the need for a series-form solution. In general, the roots of C in Eq. (49) are not periodic, which implies that the basis functions in the series-form solution are not orthonormal to each other. Therefore, the derivation of the coefficient of each basis function will be complicated and the convergence of the solution will still be open. For simplicity, this study uses the first root to demonstrate this theory. Also according to our previous works [38,20,21], the first root can provide sufficient accuracy. As the coating is much thinner than the substrate ($h_f \ll h_s$) and the thermal expansion coefficient of the substrate is larger than the coating($\alpha_s > \alpha_f$), the shearing stress at the interface should be negative which gives the constraints $sin(\xi_s Ch_s) > 0$, $cos(\xi_s Ch_s) < 0$, B > 0, and A < 0.

2.4.2. Free normal stress at the side faces

After solving C, there are three more unknowns left, A, B, and ε_u , requiring three boundary conditions. Recall that in the procedure to solve C, only the combination of Eq. (47) and (48) was used, which means that either Eq. (47) or Eq. (48) can be further used to solve other unknowns. Therefore two more boundary conditions are sufficient to solve all unknowns.

The normal stress at every point on the side faces for both the coating and substrate should be zero as there is no external load applied at the side faces. However, this condition can not be satisfied exactly due to the simplifying assumptions in Eqs. (11) and (12). Instead, relaxed boundary conditions are used,

$$\int_0^\lambda \int_{h_s}^h \sigma_{xx}^f(x=\lambda) dz dy = 0$$
(50)

and

$$\int_0^\lambda \int_0^{h_s} \sigma_{xx}^s(x=\lambda) dz dy = 0$$
 (51)

By substituting Eqs. (2), (25), (32), (33), (34), (37), and (40) into Eqs. (50), (51) combine with Eq. (47), all of the remaining unknowns can be determined:

$$A = Mh_f(\alpha_f \Delta T - \varepsilon_u) \tag{52}$$

$$B = \frac{A\cos(\xi_f Ch_f)}{\cos(\xi_s Ch_s)} \tag{53}$$

$$\varepsilon_u = \frac{\alpha_s h_s N - \alpha_f h_f M}{h_s N - h_f M} T \tag{54}$$

where

$$M = \lambda \frac{(1 - 2v^f)(1 + v^f)}{1 - v^f} [(1 - v^f)\lambda \cosh(C\lambda)\sin(\xi_f Ch_f)/\xi_f + v^f \sinh(C\lambda)\sin(\xi_f Ch_f)/\xi_f/C$$

$$+ \left[v^f \frac{1 - 2v^f}{2 - 2v^f} Ch_f - \frac{v^f \sin(\xi_f Ch_f)}{\xi_f (2 - 2v^f)} \right] [\cosh(C\lambda)\lambda + \sinh(C\lambda)/C] \right]^{-1}$$

$$N = \frac{\lambda (1 - 2v^s)(1 + v^s)}{1 - v^s} \left[\frac{(1 - v^s)\lambda \cos(\xi_f Ch_f)\sin(\xi_s Ch_s)\cosh(C\lambda)}{\xi_f \cos(\xi_f Ch_f)} \right]^{-1}$$

$$\xi_f \cos(\xi_f Ch_f) \cos(\xi_f Ch_f) \sin(\xi_s Ch_s) \cos(\xi_f Ch_f) \sin(\xi_s Ch_s) \cos(\xi_f Ch_f)}$$

$$\xi_f \cos(\xi_f Ch_f) \cos(\xi_f Ch_f) \cos(\xi_f Ch_f) \sin(\xi_f Ch_f)$$

$$V = \frac{\lambda(1 - 2v^{S})(1 + v^{S})}{1 - v^{S}} \left[\frac{(1 - v^{S})\lambda\cos(\xi_{f}Ch_{f})\sin(\xi_{S}Ch_{S})\cosh(C\lambda)}{\xi_{S}\cos(\xi_{S}Ch_{S})} + \frac{v^{S}\cos(\xi_{f}Ch_{f})\sin(\lambda)\sin(\xi_{S}Ch_{S})}{\xi_{S}C\cos(\xi_{S}Ch_{S})} - \frac{\cos(\xi_{f}Ch_{f})v^{S}\sin(\xi_{S}Ch_{S})}{2\xi_{S}(1 - v^{S})\cos(\xi_{S}Ch_{S})} \left[\lambda\cosh(C\lambda)\frac{\sinh(C\lambda)}{C}\right] + \frac{1 - 2v^{S}}{2 - 2v^{S}}Ch_{S}v^{S}\cos(\xi_{f}Ch_{f})\left[\cosh(C\lambda)\lambda + \frac{\sinh(C\lambda)}{C}\right] + Cv^{S}h_{S}\frac{E^{f}(1 + v^{S})(1 - 2v^{S})}{E^{S}(1 + v^{f})(2 - 2v^{S})}\left[1 - \cos(\xi_{f}Ch_{f})\right]\left[\cosh(C\lambda)\lambda + \frac{\sinh(C\lambda)}{C}\right]^{-1}$$

$$(56)$$

Now, the displacement field in both the coating and substrate have been solved explicitly. Then the stress field in the coating/substrate system can be determined by substituting the obtained displacement into the constitutive law as shown in Eqs. (2)–(7).

3. FE Simulation and Verification of the Theoretical Solution

To verify the proposed analytical model, a comparison will be made between the elastic field obtained in Section 2 and the FE simulations conducted using the commercial software ABAQUS 6.13. The material properties, which were extracted from literature [13], and geometric constants of the coating/substrate system used in this FE analysis are provided in Table 1 and the temperature change is set to be 40 °C.

Considering the symmetry, one quarter of the structure was simulated as shown in Fig. 4(a). The boundary conditions were set as follows: the symmetric boundary conditions were applied at both the left side face and the front side face, while the displacement along the z-direction at the bottom was fixed as shown in Fig. 4(a). Fig. 4(b) shows the mesh of the FE model where 3D stress 8-node linear brick elements were used to simulate both the coating and the substrate material. In order to improve the computational efficiency and accuracy, a gradient mesh was applied along the length, width, and thickness directions. From the plane of symmetry to the end faces, the mesh size increased from 0.21 mm to 1.05 mm. Four layers of elements with uniform thickness were used to mesh the coating while the thickness of elements in the substrate increased from 0.21 mm to 1.05 mm from the top to the bottom. In total, 19200 elements were used for the whole model.

In order to simulate the fully bonded interface between coating and substrate, a constraint was applied to tie the coating layer and substrate together. Therefore, no slipping or debonding was allowed. The displacement fields u_x and u_z after deformation under a

Table 1
Material properties and geometric constants used in the FE model.

Modulus (GPa) Poisson's Ratio		Thermal expansion coefficient (10 ⁻⁶ /°C)	Geometry (mm)				
E^f E^s	230 3.8	$ u^f $ $ u^s$	0.27 0.3	$lpha_{ m s}$	9 59.4	$2\lambda \ h_f \ h_s$	42 0.1 4.2

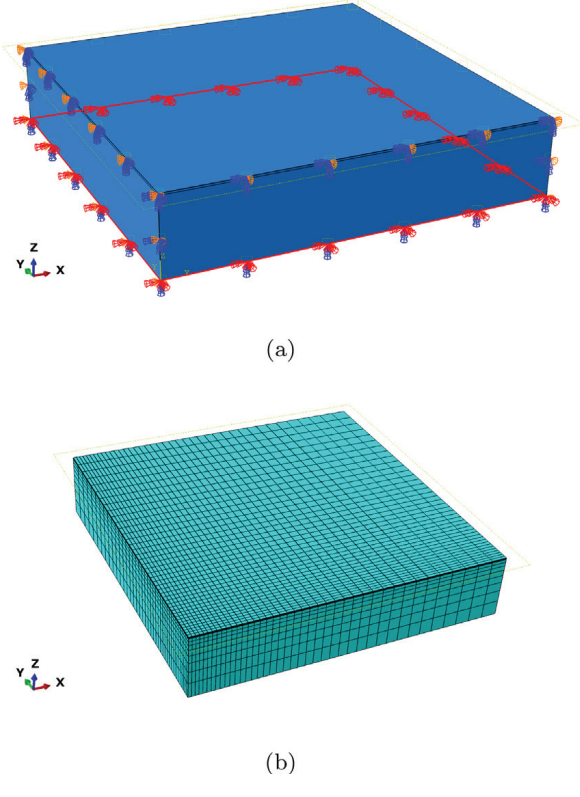


Fig. 4. FE simulation: (a) FE model and boundary conditions; and (b) mesh of the FE model.

temperature change of 40 °C are presented in Fig. 5(a) and (b) respectively. Based on the FE results, one can find that u_x is almost constant throughout the width of the structure while u_z varies in a very small range.

Fig. 6(a) shows the distribution of u_x^f across the thickness of coating with different y-coordinates. Recalling our assumption as

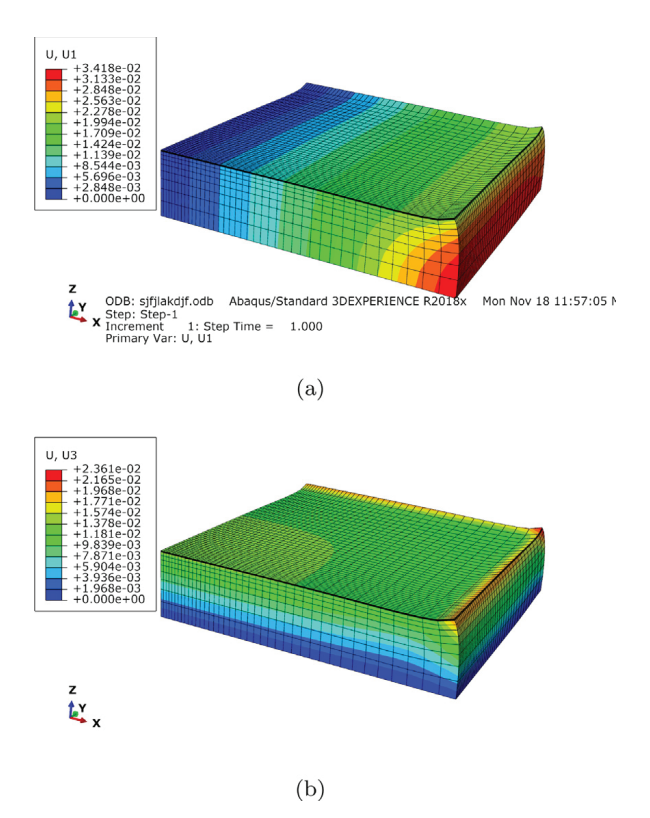
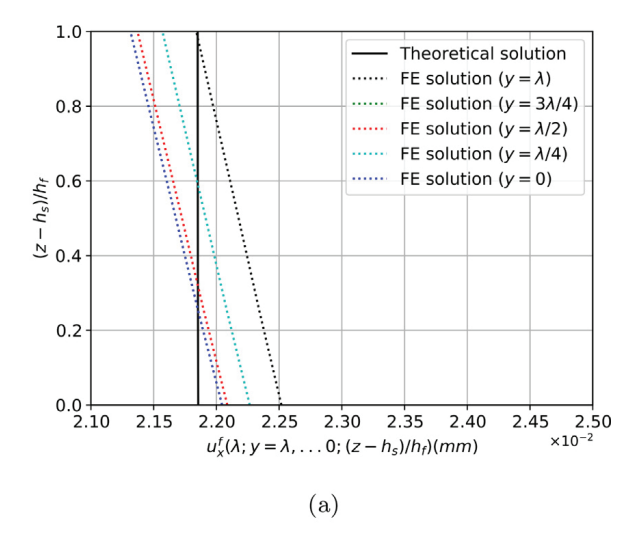


Fig. 5. Displacement field in the FE model after temperature change of 40 °C: (a) u_x . The units of displacement fields in these figures are mm.



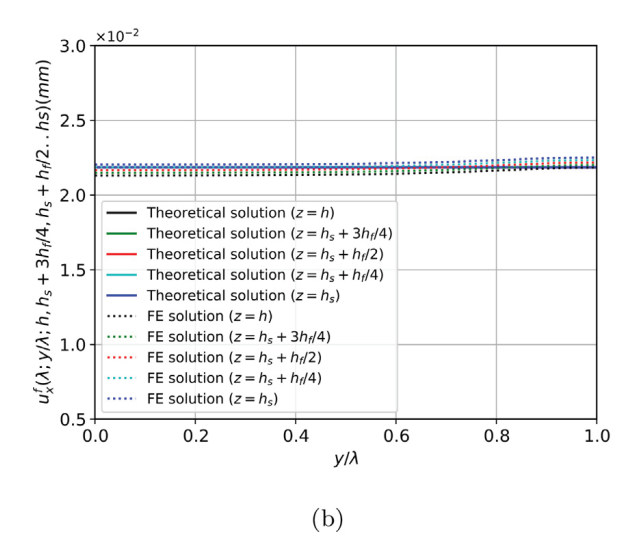


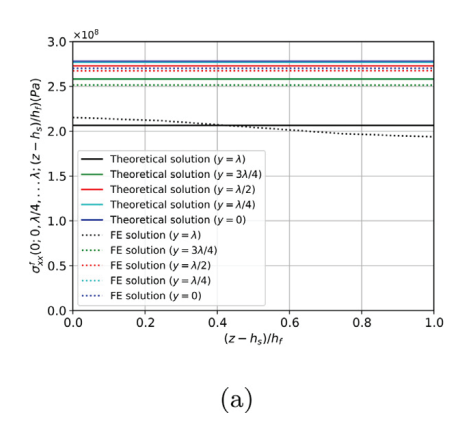
Fig. 6. Comparison between theoretical solutions and FE analysis results for u_x^f ($\Delta T = 40$ °C): (a) across thickness of coating at different y; and (b) along width direction at different depths.

shown in Eq. (12), the theoretical prediction of u_x^f is independent of y. Therefore, only one distribution of u_x^f is obtained from the theoretical model for different y-coordinates. Both the theoretical solutions and the FE analysis results show that u_x^f will decrease from the interface to the top surface of the coating because the thermal expansion coefficient of coating is much smaller than that of substrate and the effect of substrate on the deformation of the coating will reduce from the interface to the top surface of coating. Although the FE analysis results show that u_x^f will have minor changes with the change of y-coordinates, the theoretical model can still capture the distribution of u_x^f across the thickness of the coating at different y-coordinates with a maximum difference smaller than 2.5%. The distribution of u_x^f along the width direction at different depths is presented in Fig. 6(b), both theoretical solutions and FE analysis results show that u_x^f would keep constant with the change of y approximately, which means our assumption in Eq. (12) is reasonable.

Fig. 7 presents the distribution of normal stress along the x-direction in the coating (σ_x^f) . Fig. 7(a) shows that the normal stress σ_x^f will not change with depth except at the very edge and that the theoretical solutions agree well with the FE simulation results. The maximum difference between the theoretical solutions and the FE simulation results, which is reached at the edge where $y = \lambda$, is smaller than 3%. The distribution of σ_x^f along the width direction is presented in Fig. 7(b), both theoretical solution and FE simulation results show that the normal stress would decrease from the center to the edge. The difference between the simulation results and the theoretical prediction is within 2%, which denotes the accuracy of our theoretical model.

4. Fracture analysis

Consider the square section within four OMFs. When the temperature change increases to a critical value, two steady-state channeling straight cracks will initiate at the middle edge of the section. After cracking, the section is broken into four quarters, and the displacement field in each quarter can also be solved by replacing λ with $\lambda/2$ in the new local coordinate system. Therefore, the



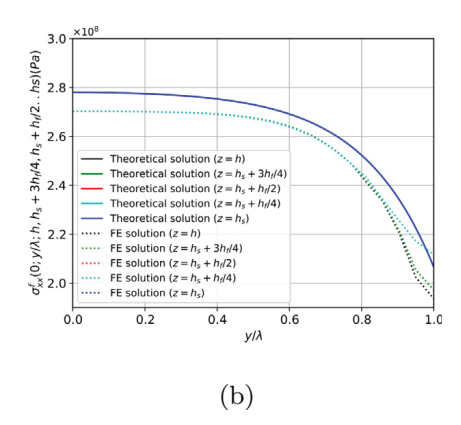


Fig. 7. Comparison between the theoretical solutions and the FE simulation results for normal stress σ_{xx}^f ($\Delta T = 40$ °C): (a) across thickness of coating at different y; and (b) along width direction at different depths.

crack opening displacement is solved. To recover this OMF, the normal stress along the central line just before the fracture initiates needs to be applied along the cracking surface. Therefore, the ERR can be obtained as the work done to close the crack opening displacement as shown in Eq. (57) [23].

$$G = \frac{1}{\lambda h_f} \int_0^{\lambda} \int_{h_s}^{h} \sigma_{xx}^f(0, y, z) [u_x^f(\lambda, h_s) - u_x^f(\lambda, z)] dz dy$$
(57)

The ERR in the coating layer will increase as the temperature change increases. Once the ERR is equal to or larger than the critical fracture ERR, a new crack will nucleate. Therefore, the following criterion is used to predict whether new fractures will infill:

$$G \geqslant G_{cr}$$
 (58)

where G_{cr} is the critical fracture ERR of the thin film.

Using the stress and displacement presented in Section 2, the ERR can be obtained through Eq. (57). Fig. 8(a) shows that when the coating thickness is constant ($h_f = 100 \,\mu\text{m}$), the ERR increases rapidly as the crack spacing increases to $6h_s$. Beyond this point, the ERR does not change any more even as the crack spacing increases. This indicates that under the temperature change ($\Delta T = 40 \,^{\circ}\text{C}$), the potential crack spacing of the given thin film ($h_f = 100 \,\mu\text{m}$, $h_s = 4.2 \,\text{mm}$) will be smaller than six times the thickness of substrate. Fig. 8(b) shows the variance of the ERR with respect to the coating thickness with constant crack spacing $\lambda = 21 \,\text{mm}$ under a temperature change of 40 °C and reveals that the ERR increases linearly as the coating thickness increases until it reaches a convex point. After this point, the ERR decreases as the coating thickness increases. At this convex point ($h_f = 120 \,\mu\text{m}$), fracture saturation is reached, therefore, no more new crack will be developed.

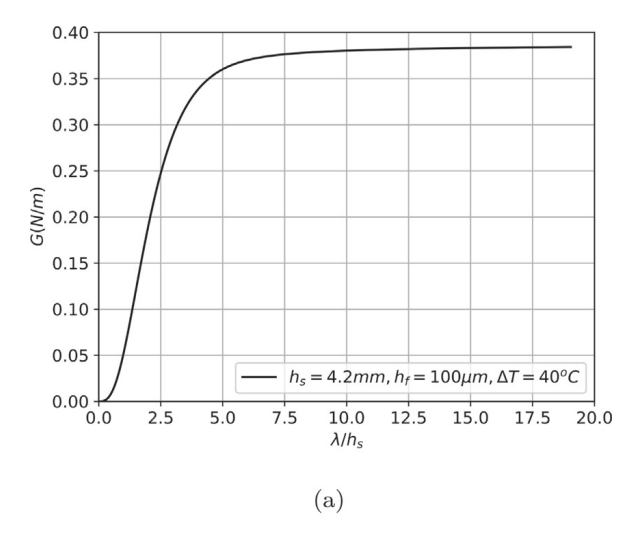
Recalling Eq. (58), when the temperature change reaches a critical value, a new OMF will nucleate. Fig. 9 illustrates the variance of required temperature changes to form a new crack in the thin film. In this study, the critical fracture ERR of the thin titania film is taken to be 0.277 J/m² [13]. Fig. 9(a) presents the required temperature change to crack the coating when the coating thickness is constant ($h_f = 100 \,\mu\text{m}$) and shows that the temperature change increases as the crack spacing decreases. When λ/h_s approaches 0.5, the temperature change turns to infinity which means no new fractures will infill and the fracture saturation is achieved. For this specified film thickness of $h_f = 100 \,\mu\text{m}$ and substrate thickness of 4.2 mm, the saturated crack spacing can be approximately evaluated as $\lambda_{cr} = 0.5h_s = 2.1 \,\text{mm}$. Fig. 9(b) shows the variance of the temperature change with respect to the coating thickness at a constant crack spacing ($\lambda = 21 \,\text{mm}$) and indicates that the required temperature change to initiate a new crack in the coating will reduce as the coating thickness decreases until a critical thickness h_{fcr} is reached. Under this critical coating thickness, the required temperature change to crack the coating increases to be infinite and the fracture saturation would be reached. For this study, the critical coating thickness is about 5 μ m when the crack spacing is 21 mm.

The variance of saturated crack spacing with respect to the coating thickness under the temperature change, $\Delta T = 40$ °C, is presented in Fig. 10 which shows that the crack spacing decreases as the thin film thickness decreases until a critical film thickness is reached. Below this thickness the crack spacing quickly increases to infinite and no new cracks will be developed, which means the fracture saturation is reached. For this case where the thickness of the substrate is 4.2 mm, the critical thickness is corresponds to about 70 μ m under the temperature change of 40 °C.

5. Verification of Fracture Analysis

5.1. FE simulation of cracking in coating

In order to verify the theoretical fracture analysis, the required temperature changes to crack the coating/substrate structures with different length but same coating thickness are validated by the FE simulations using ABAQUS. As we already know the path of cracks, the CZM is used to enable the cracking simulation. In order to reduce the effect of the cohesive element on the overall mechanical property, cohesive elements with zero thickness are inserted at the center of the coating. Fig. 11 presents the FE model



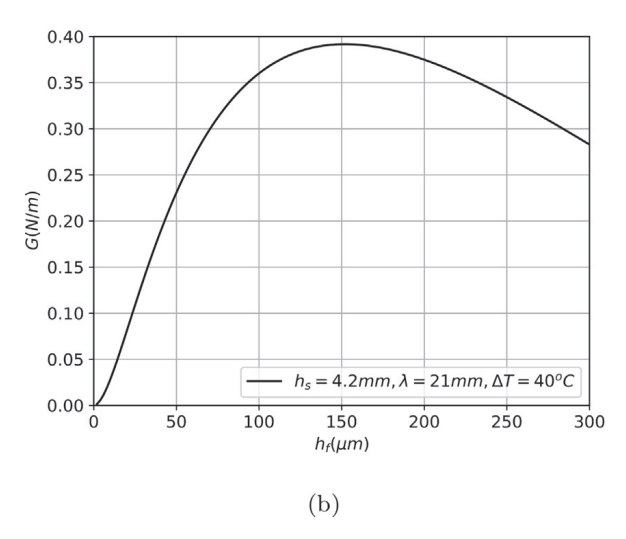


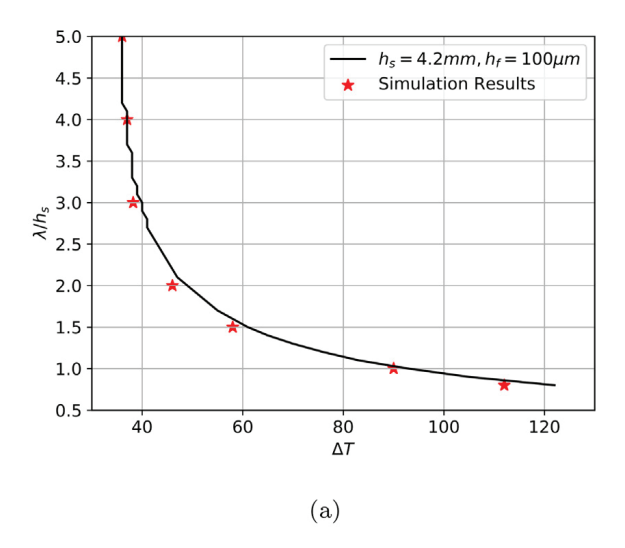
Fig. 8. Variance of ERR with respect to: (a) crack spacing; and (b) coating thickness.

and mesh, where the red dot lines indicate the locations where cohesive elements were inserted (or position where crack will be developed). The boundary conditions used in the simulation are that the lower surface of substrate is fixed along *z*-direction ($u_z^s(z=0)=0$) while the center point of the bottom of substrate is fixed to get rid of any rigid body motion.

During the FE simulations, C3D8R elements are used to simulate the solid material, while 3D cohesive elements, COH3D8, are used to simulate the cracking process. In order to increase the computational efficiency and improve the accuracy of the simulation, gradient mesh is used in the substrate across the thickness direction, while uniform sized elements are used to simulate the coating. Initially, cohesive elements with specific thickness are inserted at the center of the coating in the original part then a mesh part is created and the nodes of the cohesive elements at the two sides are edited to have the same coordinates. Thus, the zero thickness cohesive elements are created. Recall that the theoretically predicted fracture ERR is an average across the thickness of the crack surface; therefore, in order to be consistent with the theoretical model, the coating is meshed by one layer of elements.

Similarly to the solid elements, the constitutive behavior of the cohesive elements should be defined during the FE simulations. In this study, the bilinear traction-separation law is used for the cohesive element. For this bilinear traction-separation law, the initial response of the cohesive element is assumed to be linear until the damage initiation criterion is met. After that point, the stress in the cohesive elements would be released linearly until the damage evolution property is reached and the cohesive element would be damaged as shown in Fig. 12. In this constitutive model, three parameters need to be specified: the initial strength (T), the stiffness (T), and the critical fracture ERR (T). The initial strength defines the critical stress at which the cracking would initiate. Once the stress in the cohesive element reaches the initial strength, the stress would be released and the cracking would propagate once the fracture ERR reaches the critical value.

Ideally, the stiffness of the cohesive element should be infinite in order to reduce the effect of the cohesive element on the stiffness of the whole model. However, too large of a cohesive element stiffness introduces the numerical problem that the simulation can not converge. Turon et al. [50] proposed a relationship for determining the value of the stiffness for cohesive elements based on the properties of the surrounding materials as:



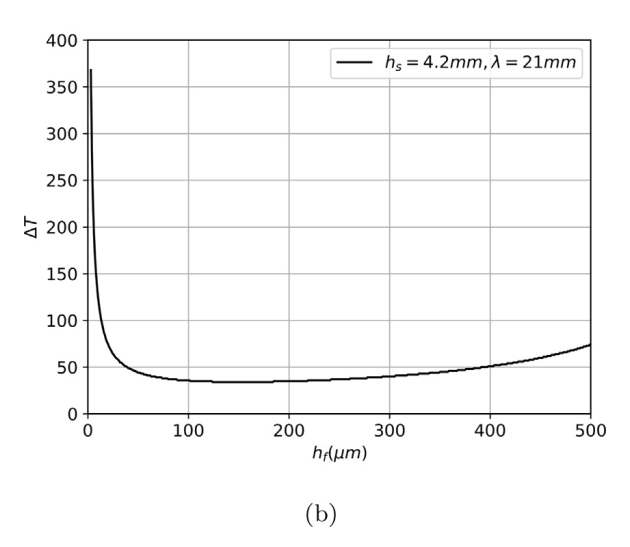


Fig. 9. Variance of required temperature change to create new cracks with respect to: (a) crack length (h_f = constant); and (b) Coating thickness (λ = constant).

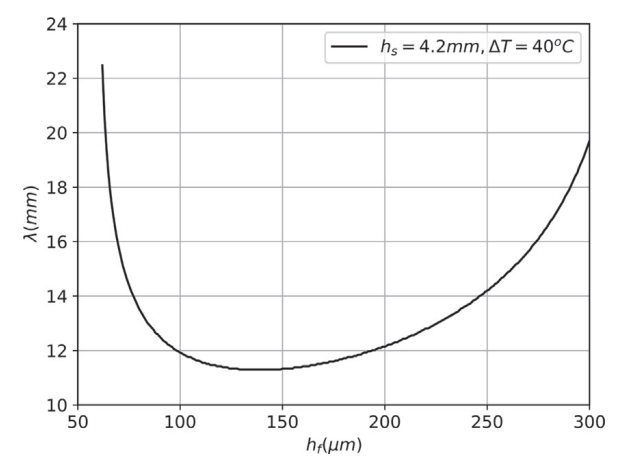


Fig. 10. Crack spacing at different coating thickness.

$$K = \frac{\alpha E}{t} \tag{59}$$

where *E* is the Young's modulus of the surrounding material, *t* is the initial thickness of the cohesive zone which is typically set to be

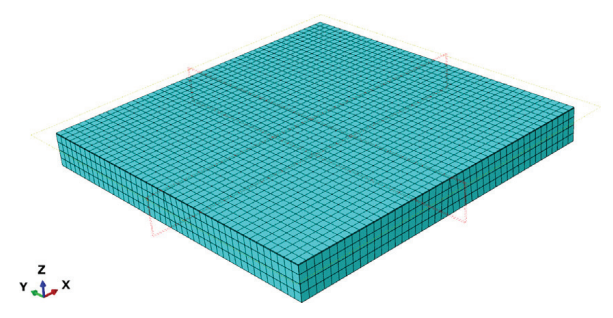


Fig. 11. FE model and mesh for cracking analysis.

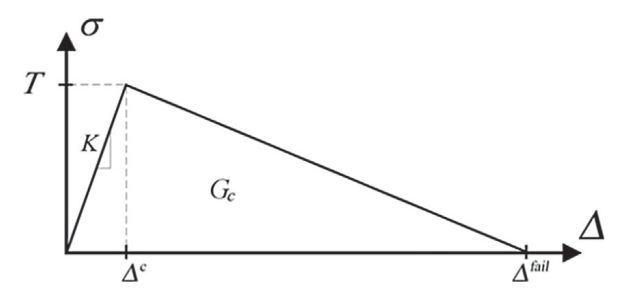


Fig. 12. Bilinear traction-separation response of the cohesive element [49].

1, and α is a parameter much larger than 1. As stated before, the stiffness of the cohesive elements should be large enough to avoid any effect on the overall compliance and should be small enough to get rid of the spurious oscillations in the tractions. Therefore, the parameter α should provide a reasonable stiffness value and a value of 50 or larger was recommended [50]. For our case, α is set to be 100, yielding a stiffness of $2.3 \times 10^7 \frac{N}{mm^3}$. The critical fracture ERR $G_{cr} = 0.277 \text{ J/m}^2$, predicted by using the cracking saturation in [13], was used in the FE simulation. The initial strength of the cohesive elements was calculated as 250 MPa by setting Δ^c as half of Δ^{fail} in Fig. 12 based on [50].

Fig. 13(a) shows the stress field (Von Mises 75% average [51]) in the coating/substrate system before the cracking initiation. Compared with the simulation results where non-cohesive elements were used, the difference is less than 1% which means the chosen stiffness of cohesive elements is reasonable. The stress field after cracking is presented in Fig. 13(b). It indicates that the stress is periodically distributed in each cracked piece. In the cracking simulation, the cohesive element deletion is enabled. Once the fracture ERR reaches the critical value, the cohesive element would be damaged and vanish, providing a way to monitor the cracking process. Based on the simulation, the cracks would initiate at the center and propagate to the edge of the coating. This is consistent with our theoretical prediction as the stress would decrease from the center to edge.

The simulated required temperature change to crack the coating with constant thickness is summarized in Table 2 and compared with the theoretical predictions in Fig. 9(a). Overall the temperature changes from the theoretical predictions agree with the simulation results well with a maximum difference of 5% at $\lambda = 0.8h_s$. In addition, the difference between the theoretical predictions and the simulation results increases as the crack spacing decreases. One potential reason is that with the decrease of crack spacing, edge effects treated approximately in our theoretical analysis would become significant. The proposed theoretical model cannot capture the stress and displacement distributions in this edge area effectively because of the application of plane and non-shearing assumptions. This problem has also been stated in [38].

5.2. Comparison with the experimental data

Recently, Roy and her colleague [47] proposed a simple model to predict the residual stress in the free expanded Galvannealed



Fig. 13. Simulated stress field in the cracking model: (a) before cracking; and (b) after cracking.

 Table 2

 Simulated temperature changes for different crack spacings.

Crack Spacing	Required Temperature Change (°C) Theoretical Predictions	Simulation Results		
$0.8h_s$	118	112		
h_{s}	94	90		
$1.5h_s$	61	58		
$2h_s$	49	46		
$3h_s$	40	38		
$4h_{\scriptscriptstyle S}$	37	37		
$5h_S$	36	36		

coating/substrate structure based on Eshelby's approach for inclusion method [52]. In this model the normal strain and normal stress caused by thermal loading were assumed to be uniformly distributed in the structure. The material properties used in this study are summarized in Table 3. Based on the obtained residual stress, the ERR in the coating along both longitudinal and transversal directions were obtained and used to predict the crack spacing. Then the crack spacing in samples with different coating thicknesses created by different thermal loadings were measured and compared with the theoretical predictions of their simplified model as shown in Table 4. Note that the predicted crack spacings from [47] all differ from the measured spacings by 50% or more. In addition, we point out that there appears to be large uncertainty in the experimentally produced crack spacings, as indicated by the fact that under almost identical conditions (e.g., samples 6 and 7), the measured spacings are about 14 and 25 μ m, respectively. Hence, our comparisons to experiment necessarily must be made only semi-quantitatively.

In the following, we use the same material properties to calculate the ERR based on the model developed here and compare the predicted crack spacing for different samples to the experimental results [47]. Note that, the Young's modulus of coating is smaller than that of substrate in this analysis. This means the coefficient of the first term in Eq. (49) is smaller than the second term, therefore, the solution of unknown C is searched near $\frac{\pi}{2h_f\xi_f}$ which make the second term of Eq. (49) be zero. Also based on the computational results, the value of the left part in Eq. (49) and the predicted crack spacing are sensitive to the vale of C. For example, when C increases by 2%, the predicted crack spacing would increase by 1.5% while the value of the left part in Eq. (49) would increase by 10% for this specific case whose material properties is shown in Table 3. Therefore, in order to predict the crack spacing accurately, C should be solved with a very high accuracy. However, as Eq. (49) is a nonlinear equation in terms of C and can only be solved numerically with some numerical errors, the presented predicted crack spacing may differ from the actual crack spacing by 1–2%.

Fig. 14 presents the change of ERR with respect to the crack spacing in different samples. For these small crack spacings, the ERR would increase with the increase of the crack spacing. Based on the literature [53], the critical fracture toughness of the δ phase Galvannealed coating is $2 \,\mathrm{MPa}\cdot\mathrm{m}^{1/2}$, then the critical fracture ERR can be calculated based on Eq. (60), where K_{lcr}^2 is the critical fracture toughness. The horizontal line in Fig. 14 shows the calculated critical fracture ERR which is equal to $28.57\,\mathrm{m}^{\mathrm{N}}$. Above this horizontal line, the ERR is higher than the critical fracture ERR, therefore, more cracks would be introduced at the center of the coating layer until the critical crack spacing, at which the ERR is smaller than or equal to the critical fracture ERR, is reached. The crack spacing at each intersection points of the horizontal line with the ERR curve for each sample shows the saturated crack spacing. These saturated crack spacing are extracted and compared with the experimental results in the literature [47], which is presented in Table 4. Note, first, that the predicted crack spacings all are approximately the correct value of 20 or more μm . The model derived here predicts crack spacings within 10% of the measured values for most conditions and it predicts that the crack spacing would decrease with the increase of temperature change or the decrease of coating thickness, which is coincident with the trends shown in Fig. 9(a) and 10. Also from Table 4, the saturated crack spacing predicted by the presented model agrees well with the experimental results, indicating that the presented model is more accurate than the model proposed by Roy [47].

$$G_{cr} = \frac{K_{l_{cr}}^2}{E^f} \tag{60}$$

6. Summary and conclusions

In this study, a 3D elastic fracture model has been presented to simulate the block cracking in the advanced polymeric solar reflectors, which is modeled by a simplified bilayer structure. The displacement field in the system under a specified temperature change is obtained theoretically. The results show that the displacement along *x*-direction is nearly constant across the width which

Table 3Material Properties and Geometric Constant [47].

Modulus (GPa)	Poisson's Ratio			Thermal expansion coefficient $(10^{-5}/^{\circ}C)$	Geometry (mm)		
E^f E^s	140 210	$ u^f $ $ v^s$	0.3 0.3	$lpha_f$ $lpha_s$	2.2 1.1	h_s	1

Table 4 Verification of crack spacing.

Sample number	1	3	2	7	6	4	5	8
Coating thickness (µm)	5.9	6.0	6.6	6.0	6.0	6.0	8.0	9.0
Temperature change (°C)	- 594	- 594	-620	-591	- 589	-576	- 595	-512
Crack spacing [47] (µm)	9.70	9.77	9.88	9.80	9.83	10.00	11.06	13.5
Observed crack spacing [47] (µm)	20.40	25.68	33.03	24.89	14.45	34.22	19.21	24.78
Crack spacing (Presented model) (µm)	21.80	21.99	22.05	22.11	22.19	22.75	25.50	31.02

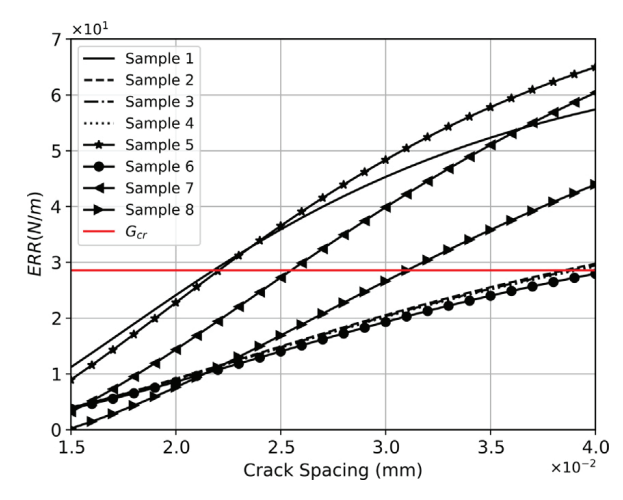


Fig. 14. Variance of ERR with respect to crack spacing for different samples.

supports our assumption that $u_{x,y} = u_{y,x}$. The obtained elastic fields were verified with FE simulations. The good agreement between theoretical predictions and simulation results (maximum difference within 3%, which is reached near the edge due to the singularity or edge effect) reveals the accuracy of the present fracture model and highlights the effectiveness of this approach.

Based on the elastic solutions, the ERR is calculated and shows that the ERR would increase rapidly as the crack spacing increases until a plateau stage is reached when the crack spacing approaches 6 times the substrate's thickness. Therefore, under the temperature change of 40 °C, coating thickness 100 μ m, and substrate thickness 4.2 mm, the potential crack spacing is smaller than 25.2 mm. When the crack spacing is constant, the ERR approximately increases linearly with the coating thickness until it reaches the convex point, at which the fracture saturation is reached. In this case ($\Delta T = 40$ °C, $\lambda = 21$ mm, $h_s = 4.2$ mm), the critical coating thickness is 120 μ m.

The fracture infilling and saturation of this specific coating/substrate system are studied based on the calculated ERR and show that, when the coating thickness remains constant, the temperature change required to form a new crack would increase as the crack spacing decreases and fracture saturation would be reached when the crack spacing approaches 0.5 times of the substrate thickness. However, when the crack spacing is constant, the required temperature change to form a new crack would decrease as the coating thickness decreases, until a critical coating thickness is reached. Under this critical thickness the required temperature change would increase to be infinite which means the fracture saturation is obtained. For the crack spacing of 21 mm, the critical coating thickness is about 5 μ m. Furthermore, the saturated crack spacing decreases linearly as the thin film thickness decreases until a critical film thickness is reached, while below this critical thickness (70 μ m), no new cracks will be developed. This trend is consistent with our previous studies [20,21]. In order to verify the theoretical fracture analysis, FE simulations based on CZM with bilinear traction-separation constitutive behavior were conducted. The simulated temperature changes needed to initiate a new crack in the coating with different crack spacing but constant coating thickness were compared with the theoretical predictions. The good agreement between the simulation results and the theoretical solutions indicates the accuracy of the proposed fracture model. Furthermore, the predicted crack spacing in samples with various coating thicknesses under different temperature changes are compared with the experimental data from literature. The results show that the presented fracture model gives a more accurate prediction on the crack spacing than the model proposed in the literature.

Overall, the presented model is able to capture the displacement and stress distributions in the coated structure accurately and predict the fracture initiation, infilling, and saturation successfully. The present formulation is general and can be applied to other types of coating/substrate systems.

Declaration of Competing Interest

None.

Acknowledgments

This work was supported by the U.S. Department of Energy under Contract No. DE-AC36- 08-GO28308 with the National Renewable Energy Laboratory through the DOE SETP program and the U.S. National Science Foundation under award No. 1738802 with the Center for Energy Harvesting Materials and Systems through NSF Industry/University Cooperative Research Center Program. The U.S. Government retains and the publisher, by accepting the article for publication, acknowledges that the U.S. Government retains a nonexclusive, paid-up, irrevocable, worldwide license to publish or reproduce the published form of this work, or allow others to do so, for U.S. Government purposes.

Appendix A. Supplementary material

Supplementary data associated with this article can be found, in the online version, at https://doi.org/10.1016/j.engfracmech.

References

- [1] Wang D, Peng H, Liu J, Yao C. Wear behaviour and microstructural changes of SiCw-Al composite under unlubricated sliding friction. Wear 1995;184(2):187-92.
- [2] Sreevatsa S. Carbon nanotube electronic structures as anti-corrosion coatings; 2009.
- [3] Bele E, Bouwhuis B, Codd C, Hibbard G. Structural ceramic coatings in composite microtruss cellular materials. Acta Mater 2011;59(15):6145-54.
- [4] Chen Y, Reed R, Marquis E. As-coated thermal barrier coating: structure and chemistry. Scripta Mater 2012;67(9):779-82.
- [5] Fu Y, Du H, Huang W, Zhang S, Hu M. Tini-based thin films in mems applications: a review. Sens Actuat A: Phys 2004;112(2-3):395-408.
- [6] Kennedy C, Terwilliger K, Milbourne M. Development and testing of solar reflectors. Presented at the 2004 DOE solar energy technologies review meeting; 2004.
- [7] Park J-S, Chae H, Chung HK, Lee SI. Thin film encapsulation for flexible am-oled: a review. Semicond Sci Technol 2011;26(3):034001.
- [8] Guo CF, Sun T, Liu Q, Suo Z, Ren Z. Highly stretchable and transparent nanomesh electrodes made by grain boundary lithography. Nat Commun 2014;5:3121.
- [9] Jorgensen G, Gee R, DiGrazia M. Development and testing of abrasion resistant hard coats for polymer film reflectors. Presented at 16th SolarPACES Conference. 2010.
- [10] Sutter F, Ziegler S, Schmücker M, Heller P, Pitz-Paal R. Modelling of optical durability of enhanced aluminum solar reflectors. Sol Energy Mater Sol Cells 2012;107(C):37–45.
- [11] Sansom C, Fernández-García A, Sutter F, Almond H, King P, Martínez-Arcos L. Soiling and cleaning of polymer film solar reflectors. Energies 2016;9(12):1006.
- [12] Cheacharoen R, Mateker WR, Zhang Q, Kan B, Sarkisian D, Liu X, et al. Assessing the stability of high performance solution processed small molecule solar cells. Sol Energy Mater Sol Cells 2017;161(C):368–76.
- [13] Zhang C, Gray MH, Tirawat R, Larsen RE, Chen F. Effects of uv aging on the cracking of titanium oxide layer on poly (ethylene terephthalate) substrate: Preprint. Tech rep., NREL (National Renewable Energy Laboratory (NREL), Golden, CO (United States)); 2016.
- [14] Stach M, Lo C-Y. Nano metal crack initiation on polymer and its optical application with tunable metal dimensions. 14th IEEE International conference on nanotechnology. IEEE; 2014. p. 424–7.
- [15] Xia ZC, Hutchinson JW. Crack patterns in thin films. J Mech Phys Solids 2000;48(6):1107-31.
- [16] Agrawal DC, Raj R. Measurement of the ultimate shear strength of a metal-ceramic interface. Acta Metall 1989;37(4):1265-70.
- [17] Chai H. Channel cracking in inelastic film/substrate systems. Int J Solids Struct 2011;48(7):1092-100.
- [18] Zhang C, Chen F, Gray MH, Tirawat R, Larsen RE. An elasto-plastic solution for channel cracking of brittle coating on polymer substrate. Int J Solids Struct 2017;120:125–36.
- [19] Musil J, Sklenka J, Prochazka J. Protective overlayer coating preventing cracking of thin films deposited on flexible substrates. Surf Coat Technol 2014;240:275–80.
- [20] Chen F, He X, Prieto-Munoz P, Yin H. Opening-mode fractures of a brittle coating bonded to an elasto-plastic substrate. Int J Plast 2015;67:171–91.
- [21] He X, Chen F, Yin H. Opening-mode micro-cracking in brittle coatings on ductile wires/rods. Int J Damage Mech 2016. 1056789516659330.
- [22] Nakamura T, Kamath SM. Three-dimensional effects in thin film fracture mechanics. Mech Mater 1992;13(1):67–77.
- [23] Beuth J. Cracking of thin bonded films in residual tension. Int J Solids Struct 1992;29(13):1657-75.
- [24] Suo Z, Hutchinson JW. Steady-state cracking in brittle substrates beneath adherent films. Int J Solids Struct 1989;25(11):1337–53.
- [25] Ye T, Suo Z, Evans A. Thin film cracking and the roles of substrate and interface. Int J Solids Struct 1992;29(21):2639-48.
- [26] Beuth J, Klingbeil N. Cracking of thin films bonded to elastic-plastic substrates. J Mech Phys Solids 1996;44(9):1411–28.
- [27] Li J, Chou T-W. Elastic field of a thin-film/substrate system under an axisymmetric loading. Int J Solids Struct 1997;34(35):4463-78.
- [28] Hsueh C, Yanaka M. Multiple film cracking in film/substrate systems with residual stresses and unidirectional loading. J Mater Sci 2003;38(8):1809-17.
- [29] Wellner P, Kraft O, Dehm G, Andersons J, Arzt E. Channel cracking of β-NiAl thin films on si substrates. Acta Mater 2004;52(8):2325–36.
 [30] Thouless M, Li Z, Douville N, Takayama S. Periodic cracking of films supported on compliant substrates. J Mech Phys Solids 2011;59(9):1927–37.
- 131] Chai H, Fox J. On delamination growth from channel cracks in thin-film coatings. Int J Solids Struct 2012;49(22):3142–7.
- [32] Yin HM. Opening-Mode cracking in asphalt pavements: crack initiation and saturation. Road Mater Pavement Des 2010;11(2):435-57.
- [33] Bai T, Pollard D, Gao H. Explanation for fracture spacing in layered materials. Nature 2000;403(6771):753-6.
- [34] Bai T, Pollard DD, Gross MR. Mechanical prediction of fracture aperture in layered rocks. J Geophys Res: Solid Earth (1978, 2012) 2000;105(B1):707–21.
- [35] Bai T, Pollard DD. Spacing of fractures in a multilayer at fracture saturation. Int J Fract 100 (4).
- [36] Yin H, Paulino G, Buttlar W. An explicit elastic solution for a brittle film with periodic cracks. Int J Fract 2008;153(1):39-52.
- [37] Yin H. Fracture saturation and critical thickness in layered materials. Int J Solids Struct 2010;47(7):1007–15.
- [38] Yin HM, Prieto-Munoz PA. Stress transfer through fully bonded interface of layered materials. Mech Mater 2013;62:69–79.
- [39] Stoney GG. The tension of metallic films deposited by electrolysis. Proc Roy Soc Lond. Ser A, Contain Papers Math Phys Charact 1909;82(553): 172-5.
- [40] Berry B. Anelastic relaxation and diffusion in thin-layer materials. Noyes Data Corp, Diffusion Phenom Thin Films Microelectron Mater 1989:73-145.
- [41] Ohring M. Materials science of thin films. Academic press; 2001.
- [42] Schwarzer N, Richter F. On the determination of film stress from substrate bending: Stoney's formula and its limits. Tech rep, University of Chemnitz; 2006.
- [43] Evans A, Hutchinson J. The thermomechanical integrity of thin films and multilayers. Acta Metall Mater 1995;43(7):2507–30.
 [44] Hutchinson JW. Stresses and failure modes in thin films and multilayers, Notes for a Dcamm Course. Technical University of Denmark, Lyngby; 1996. p. 1–45.
- [45] Zhang X, Wu Y, Xu B, Wang H. Residual stresses in coating-based systems, part i: mechanisms and analytical modeling. Front Mech Eng China 2007;2(1):1–12.
- [46] Ahmed F, Bayerlein K, Rosiwal S, Göken M, Durst K. Stress evolution and cracking of crystalline diamond thin films on ductile titanium substrate: analysis by micro-raman spectroscopy and analytical modelling. Acta Mater 2011;59(14):5422–33.
- [47] Roy U, Ghosh C. Residual stress analysis in galvannealed coating. Ironmak Steelmak 2016;43(6):465-72.
- [48] Hsueh C, Wereszczak A. Multiple cracking of brittle coatings on strained substrates. J Appl Phys 2004;96(6):3501-6.
- [49] Song K, Dávila CG, Rose CA. Guidelines and parameter selection for the simulation of progressive delamination. In: ABAQUS User's Conference, Vol. 41; 2008. p. 43-4.
- [50] Turon A, Camanho PP, Costa J, Dávila C. A damage model for the simulation of delamination in advanced composites under variable-mode loading. Mech Mater 2006;38(11):1072–89.
- [51] Mises Rv. Mechanik der festen k\u00f6rper im plastisch-deformablen zustand. Nachrichten von der Gesellschaft der Wissenschaften zu G\u00f6ttingen, Mathematisch-Physikalische Klasse 1913;1913(4):582–92.
- [52] Eshelby J. The determination of the elastic field of an ellipsoidal inclusion, and related problems. Proc Royal Soc Lond. Ser A, Math Phys Sci 1957.p. 376–96.
- [53] Iost A, Foct J. Toughness and residual stresses in galvanizing coatings. J Mater Sci Lett 1993;12(17):11340-3.